CHEMISTRY OF MATERIALS

pubs.acs.org/cm

Article

Understanding the Prospects of the Thermoelectric Performance of the $YbMg_2(Bi,Sb)_2$ Zintl Phase

Published as part of Chemistry of Materials special issue "Honoring the Outstanding Contributions of Mercouri Kanatzidis to Chemistry of Materials."

Kushal Mehrotra, Andrei Novitskii,* and Takao Mori*

Cite This: *Chem. Mater.* 2025, 37, 6782–6790

Read Online

ACCESS | Metrics & More | Article Recommendations | Supporting Information

ABSTRACT: AM_2X_2 Zintl compounds, crystallizing in layered structures, have recently garnered attention due to their promising thermoelectric properties. In this study, we explore the chemical bonding and elastic and thermoelectric properties evolution across the full $YbMg_2Bi_{2-x}Sb_x$ solid solution. The transition from $YbMg_2Bi_2$ to $YbMg_2Sb_2$ leads to a continuous linear chemical-bond shortening and thus a significant enhancement in elastic moduli and sound velocity, resulting in overall significant lattice stiffening. Simultaneously, the shift toward more ionic chemical bonding leads to significant changes in the band structure, particularly an increase in effective mass and a decrease in both carrier concentration and mobility, which in turn reduces the power factor for Sb-rich samples. However, a rapid increase in point-defect scattering causes the lattice thermal conductivity to drop from ≈3 to almost 1 $Wm^{-1-}K^{-1}$ at 300 K for the intermediate compositions, thus opening new room for further optimization of the Sb-rich representatives of the $YbMg_2Bi_{2-x}Sb_x$. Therefore, in this work, we have demonstrated that despite the seemingly intrinsically higher thermoelectric performance in the Bi-rich region of the $YbMg_2Bi_{2-x}Sb_x$ solid solution, the Sb-rich representatives may in fact be even more promising due to better mechanical and thermal stability and greater room for further charge carrier concentration optimization.

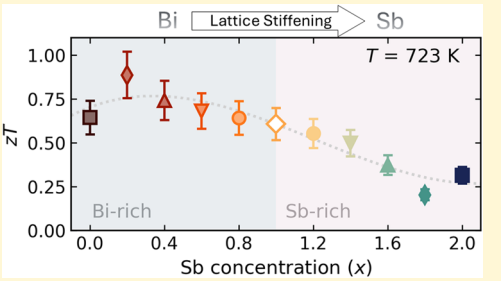

INTRODUCTION

Thermoelectric (TE) devices offer a solid-state means to convert heat into electricity, holding promise for waste heat recovery and refrigeration applications.[1] The conversion efficiency of a TE device is governed by the dimensionless figure of merit (zT) of a material used as a working body.[2] In turn, $zT = \alpha^2\sigma T/\kappa_{tot}$, where α is the Seebeck coefficient, σ is the electrical conductivity, T is the absolute temperature, and $\kappa_{tot} = \kappa_{lat} + \kappa_{el}$ is the total thermal conductivity, representing the sum of the lattice and electronic thermal conductivities, respectively.[3] Achieving a high zT requires a large power factor ($\alpha^2\sigma$) and low κ_{tot}, which is not a trivial task since α, σ, and κ_{tot} are inherently interdependent.

Zintl phases have emerged as promising TE materials in this context, as their intrinsically low κ_{lat} and complex crystal and electronic structures make it possible to decouple electronic and thermal transport.[4,5] In particular, layered AM_2X_2 compounds (where A is a divalent cation, M a metallic element, and X a pnictogen) crystallizing in the $CaAl_2Si_2$-type structure have drawn extensive interest.[6] These compounds consist of covalent two-dimensional $[M_2X_2]^{2-}$ (M = Mg, Zn, Cd; X = Sb, Bi) anionic slabs sandwiched between A^{2+} (A = Ca, Mg, Eu, Yb) cation monolayers, and many exhibit excellent TE performance (for example, AZn_2Sb_2, Mg_3Sb_2, and AMg_2Bi_2 families).[7−9]

Many of the highest zT results among AM_2X_2 type Zintl compounds were obtained via isoelectronic substitution or alloying on the cation sublattices, increasing carrier mobility and/or inducing band convergence.[4,7] AMg_2Bi_2-based compounds, in particular, have been recently reported to achieve $zT \approx 1.3$ at 873 K without the use of toxic elements (e.g., in $Eu_{0.2}Yb_{0.2}Ca_{0.8}Mg_2Bi_2$).[10] $YbMg_2Bi_2$ in particular has shown competitive thermoelectric performance in recent years (e.g., $YbMg_2Bi_{1.58}Sb_{0.4}$ with $zT \approx 1$ at 873 K).[11,12] Yet, Bi-rich Zintl phases generally exhibit weaker chemical bonding compared to their Sb-rich counterparts,[6,13] owing to the larger atomic radius and lower electronegativity of Bi.[14,15] Such a softly bonded lattice typically results in a low Young's modulus, thus lower κ_{lat}, but also poor mechanical and thermal stability.[12,16,17] In the case of $YbMg_2Bi_2$, their weakly bonded interlayers can lead

Received: June 11, 2025
Revised: July 28, 2025
Accepted: August 13, 2025
Published: August 26, 2025

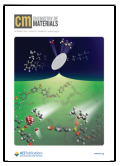

to microstructural instability at high temperatures (e.g., the emergence of voids or phase segregation upon long-term annealing), surface oxidation, and deterioration when exposed to air or water, ultimately degrading its transport properties.[11,12] These reliability challenges underscore a need to balance intrinsic TE performance with mechanical robustness and chemical stability in Bi-rich Zintl phases.

$YbMg_2Sb_2$, in turn, is a poor conductor exhibiting very high resistivity and a large Seebeck coefficient when undoped due to its semiconducting nature.[18] At the same time, $YbMg_2Sb_2$ has significantly shorter Yb−Sb and Mg−Sb bonds (higher bond energy) than the corresponding bonds in $YbMg_2Bi_2$. Strengthening the bonding is counter to the conventional strategy of lattice softening,[16] yet it directly addresses the stability and durability concerns. Consequently, strengthening the lattice by partial Sb substitution on the Bi sublattice is one of the promising approaches to overcoming the processing/handling and stability issues of $YbMg_2Bi_2$. Recent studies by Wang et al. and Liang et al. have provided new insights into the effects of Sb alloying in $YbMg_2Bi_2$, demonstrating that a moderate increase in bonding strength can considerably improve the material's resistance to thermal degradation and mechanical failure.[11,12] Ab initio calculations and sound velocity measurements confirm that replacing Bi with Sb stiffens the lattice in the $YbMg_2Bi_{2-x}Sb_x$ solid solutions. In addition, Sb-alloyed samples were found to better preserve their TE properties after long-term heating, whereas Bi-rich samples suffered noticeable performance degradation. This evidence illustrates that chemical-bond strengthening via Sb substitution can yield a more robust thermoelectric material without sacrificing efficiency, providing a valuable design strategy for practical applications. To date, studies on the $YbMg_2(Bi,Sb)_2$ system have largely focused on keeping the anion entity fixed to be either Bi or Sb, while substituting Yb and/or Mg-site with isovalent elements. To the best of our knowledge, only two studies, by Wang et al.[11] and Liang et al.,[12] have investigated Bi to Sb substitution. However, due to the increased porosity in Sb-rich samples as mentioned by Wang et al.,[11] their investigation was limited to $x = 0.4$ in Sb content in $YbMg_2Bi_{1.98-x}Sb_x$. However, a comprehensive investigation of the solid solution series $YbMg_2Bi_{2-x}Sb_x$ is important for elucidating the continuous evolution of the material's transport, structural, and mechanical properties. Such an investigation can reveal whether any intermediate compositions offer superior trade-offs, e.g., an optimal alloy that maximizes phonon scattering while maintaining sufficient carrier mobility, or any nonlinear effects (e.g., band convergence or even structural transitions) that occur at certain Bi/Sb ratios.

In this work, we present a systematic study of the $YbMg_2(Bi,Sb)_2$ solid solution covering the entire range from $YbMg_2Bi_2$ to $YbMg_2Sb_2$. A series of polycrystalline $YbMg_2Bi_{2-x}Sb_x$ samples was synthesized and characterized to evaluate how gradually substituting Bi for Sb affects the material's thermoelectric and elastic properties as well as chemical bond strength. We reveal the relationship between anion composition and key transport properties, as well as material hardness and elastic properties. The insights gained here not only demonstrate the tunability of $YbMg_2(Bi,Sb)_2$ materials for improved zT and durability but also may guide further improvement in the Sb-rich end (e.g., through doping, band structure modifications, or microstructural engineering) to advance these Zintl phases toward practical thermoelectric applications.

MATERIALS AND METHODS

Synthesis. Bulk polycrystalline samples with nominal compositions of $YbMg_2Bi_{2-x}Sb_x$ (x = 0, 0.2, 0.4, 0.6, 0.8, 1, 1.2, 1.4, 1.6, 1.8, and 2) were synthesized using mechanochemical synthesis, followed by densification via spark plasma sintering (SPS). Ytterbium ingots (Yb, Alfa Aesar, 99.9%), bismuth chunks (Bi, 5N Plus, ≥99.999%), antimony shots (Sb, Sigma-Aldrich, 99.999%), and magnesium turnings (Mg, Sigma-Aldrich, 99.95%) were weighed according to the stoichiometric ratios and loaded into a stainless steel milling jar along with two 1/2-in. diameter stainless steel balls inside an Ar-filled glovebox with oxygen and water vapor levels below 5 ppm. Subsequently, the mixtures were subjected to high-energy ball milling in an 8000D Mixer/Mill (SPEX SamplePrep). Based on previous reports[11,12,19] and preliminary ball milling process optimization (Figures S1−S3), 12 h of milling with a ball-to-powder ratio of 16:7 was used to ensure phase formation and reproducibility. All of the as-milled powders were consolidated via SPS (322 LX, Fuji-SPS, Japan) at 873 K for 5 min in a Ø10 mm graphite die under 50 MPa uniaxial pressure in Ar atmosphere with heating and cooling rates of 100 and 25 K min^{-1}, respectively. The densified pellets were then annealed at 773 K for 10 h in an evacuated quartz tube.

Structural and Chemical Characterization. PXRD patterns were collected at room temperature using a MiniFlex diffractometer (Rigaku, Japan) with Cu−K_α radiation (λ = 1.5406 Å). Lattice parameters were calculated through Rietveld refinement of PXRD patterns by using the FullProf software package.[20] The microstructure and elemental composition of the sintered samples were examined by field emission scanning electron microscopy (FESEM; Hitachi SU8230, Japan) in conjunction with an energy-dispersive X-ray spectroscopy (EDS) detector (X-Max^N, Horiba Scientific, Japan).

Elastic Moduli and Sound Velocity. To investigate elastic moduli, the longitudinal (ν_l) and transverse (ν_t) sound velocities of $YbMg_2Bi_{2-x}Sb_x$ were measured by a sing-around ultrasonic velocity measuring instrument (UVM-2, Ultrasonic Engineering Co., Japan) at room temperature. The Young's (E), bulk (K), and shear (G) moduli were calculated as

$$E = \frac{d\nu_t^2(3\nu_l^2 - 4\nu_t^2)}{\nu_l^2 - \nu_t^2}$$
$$K = d\left(\nu_l^2 - \frac{4}{3}\nu_t^2\right), \text{ and } G = \nu_t^2 d \quad (1)$$

where d is the sample density measured through the Archimedes method with ethanol as the working fluid. In the Debye model, the phonon density of states (pDOS) scales as $g(\omega) \propto \omega^2/v^3$, so that each acoustic branch enters thermodynamic and transport integrals with a weight v^{-3}.[21,22] Accordingly, the average sound velocity v_a is taken as the cubic-harmonic mean

$$v_a = \left[\frac{1}{3}\left(\frac{1}{v_l^3} + \frac{2}{v_t^3}\right)\right]^{-1/3} \quad (2)$$

which properly accounts for one longitudinal and two transverse modes in proportion to their contributions to the total pDOS.[23]

Vickers Hardness Measurement. Vickers hardness of each sample was measured via the indentation method using a micro Vickers hardness tester (HMV-G31, Shimadzu Co., Japan) on the surface of polished samples under a load of F = 1.961 N and a hold time of 10 s per measurement. Vickers hardness values were calculated as HV = $1.891F/(2l)^2$ ($2l$ is the diagonal length of the indent). To get a constant average value and the respective error bar, at least 5 indents were collected.

Thermal Property Measurement. The total thermal conductivity (κ_{tot}) was estimated through the well-known formula $\kappa_{tot} = \chi C_p d$, where χ is the thermal diffusivity and C_p is the specific heat

https://doi.org/10.1021/acs.chemmater.5c01433
Chem. Mater. 2025, 37, 6782−6790

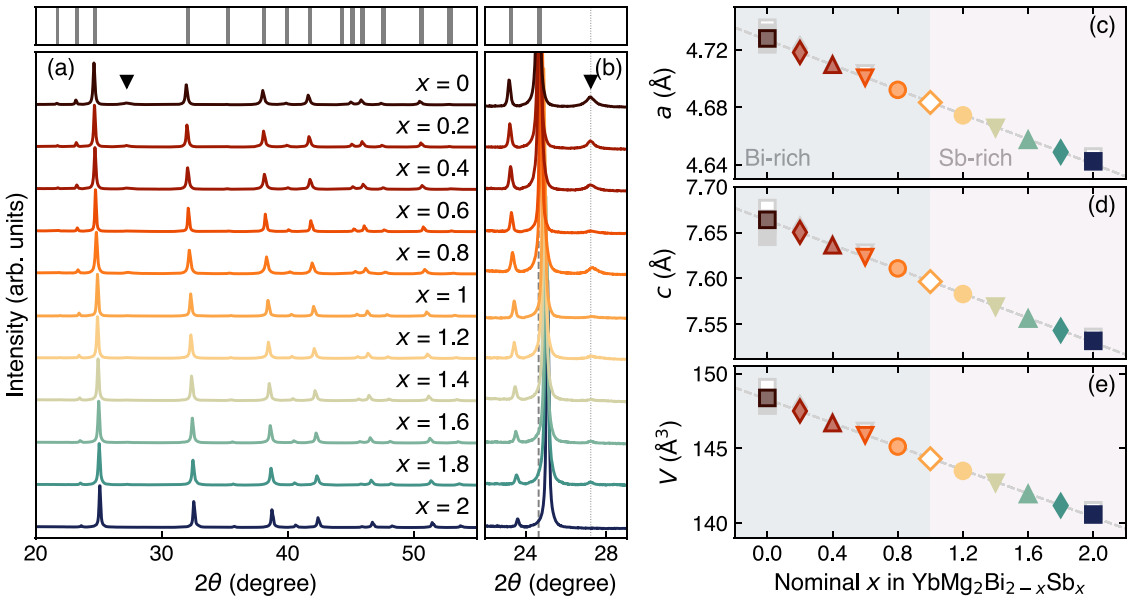

Figure 1. (a) Room-temperature powder X-ray diffraction patterns for $YbMg_2Bi_{2-x}Sb_x$ (x = 0, 0.2, 0.4, 0.6, 0.8, 1, 1.2, 1.4, 1.6, 1.8, 2) samples after spark plasma sintering and annealing. (b) Enlarged section of part (a) in a 2θ range from 22 to 29°, where the Bi secondary phase has the most intensive reflection indicated by a black solid triangle (▼). Bragg's reflections for the $YbMg_2Bi_2$ phase, taken from ref 24 are indicated by gray ticks on the top part of the figure. The lattice parameters (c) a, (d) c, and (e) unit cell volume V of $YbMg_2Bi_{2-x}Sb_x$ are shown as a function of increasing nominal Sb content. The a and c parameters experience a slight linear contraction of ~2% in good agreement with Vegard's law, resulting in a ~5% shrinkage of the unit cell volume V. Reference data shown in parts (c–e) taken from refs 11,12,18,24–26 (open gray symbols for polycrystals and filled gray symbols for single crystals, respectively).

capacity. The thermal diffusivity χ was measured on graphite-coated disk-shaped samples using the laser flash technique (LFA 467 Hyperflash, Netzsch, Germany) and analyzed using a modified Cape–Lehman model with pulse correction.[27] The C_p was approximated using the model proposed by Agne et al. and calculated for each composition.[28] The lattice thermal conductivity (κ_{lat}) was calculated from κ_{tot} by subtracting the electronic contribution (κ_{el}) estimated according to the Wiedemann–Franz law, where $\kappa_{el} = \sigma LT$. L is the Lorenz number derived from the Seebeck coefficient (α) as $L = 1.5 + \exp\{-|\alpha|/116\}$ in the framework of the effective mass model with transport in a single parabolic band limited by acoustic phonon scattering (SPB-APS).[29]

Electrical Transport and Hall Measurements. The Seebeck coefficient (α) and electrical conductivity (σ) were simultaneously measured on rectangular bars using a commercial apparatus (ZEM-3, ULVAC Inc., Japan) under partial He pressure. Electrical resistivity and Hall effect measurements were performed at room temperature using a standard five-probe configuration implemented in a physical properties measurement system (PPMS9T, Quantum Design Inc.). Electrical contacts were made with a 0.05 mm platinum wire and silver paste (Ted Pella, Inc.). A thin layer of gold was predeposited onto the contact area to improve electrical contact. The Hall coefficient (R_H) was obtained from the linear fit of the magnetic field dependence of the Hall resistivity in a range from ±5 T. The charge carrier concentration (n) was also calculated assuming SPB-APS as $n = r_H/eR_H$, with e representing the elemental charge, and r_H representing the Hall factor, which depends on the chemical potential and carrier scattering mechanism. Charge carrier mobility (μ) was calculated as $\mu = \sigma = R_H/r_H$. Samples were slightly polished prior to each measurement. Between measurements, the samples were kept in a desiccator under a static vacuum of $\approx 2.5 \times 10^{-3}$ mbar.

The uncertainty of the Hall measurements was estimated to be in a range from 5 to 10%, 6% for the Seebeck coefficient, 8% for the electrical conductivity, 11% for the thermal conductivity, and 16% for the figure of merit zT.[30] Error bars are not shown in some figures to improve the readability.

RESULTS AND DISCUSSION

Phase Identification and Microstructural Analysis. The room-temperature powder X-ray diffraction (PXRD) patterns of polycrystalline $YbMg_2Bi_{2-x}Sb_x$ samples are shown in Figure 1a. The main diffraction peaks for all compositions correspond to the $YbMg_2(Bi,Sb)_2$ phase with a trigonal $CaAl_2Si_2$-type crystal structure (space group $P\bar{3}m1$).[24] A weak reflection near $2\theta \approx 27°$ is observed in all samples except for the pure $YbMg_2Sb_2$ end-member (x = 2), as highlighted in Figure 1b. Within the detection limits of PXRD, this peak is attributed to residual Bi, typically observed as a secondary phase in this family of compounds.[11,12,25,26,31,32] With increasing Sb content, the main diffraction peaks shift systematically toward higher 2θ values (Figure 1b), indicating a linear decrease in lattice parameters in agreement with Vegard's law (Figure 1c,d). This behavior is consistent with the smaller atomic radius of Sb (1.45 Å) compared to Bi (1.60 Å),[33] and confirms the successful substitution of Sb at the Bi site, forming a complete solid solution across the $YbMg_2Bi_{2-x}Sb_x$ series. The qualitative analysis was further validated by Rietveld refinement (Table S1 and Figure S4), which quantitatively confirms the monotonic decrease in lattice constants and the associated contraction of the unit cell volume (Figure 1e). The refined lattice parameters for pristine $YbMg_2Bi_2$ and $YbMg_2Sb_2$ agree well with previously reported values.[12,24,25]

All $YbMg_2(Bi,Sb)_2$ samples exhibit a fine and dense microstructure, typical for Zintl compounds, obtained by high-energy ball milling, followed by spark plasma sintering. The relative density was measured to be above 95% of the theoretical density (Table S1) for all of the samples. EDS analysis, in turn, confirms the presence of relatively small in size (much less than ≈1 μm) Bi inclusions, while also revealing a small amount of rather large (tens of microns) MgO

https://doi.org/10.1021/acs.chemmater.5c01433
Chem. Mater. 2025, 37, 6782–6790

inclusions that were not detected by XRD. As mentioned above, such secondary phases are typically observed in these compounds, yet they are difficult to detect due to the high reactivity and susceptibility of the material to oxidation and reaction with water, which complicates measurements and accurate SEM surface analysis.[25] At the same time, the actual composition of main phase $YbMg_2(Bi,Sb)_2$ is confirmed to be close to the nominal one, with a uniform distribution of the constituent elements (Figures S5–S7).

Composition-Dependent Elastic Properties. As mentioned above, the unit cell volume (Figure 1e) and thus average bond length decrease with Sb content. As a result, Young's modulus, as well as bulk and shear moduli, increase linearly with increasing x due to Mg–(Bi,Sb) bonds becoming shorter[13,34] and show an ≈45% increase with transition from $YbMg_2Bi_2$ to $YbMg_2Sb_2$ (Figure 2a), which is quite noticeable

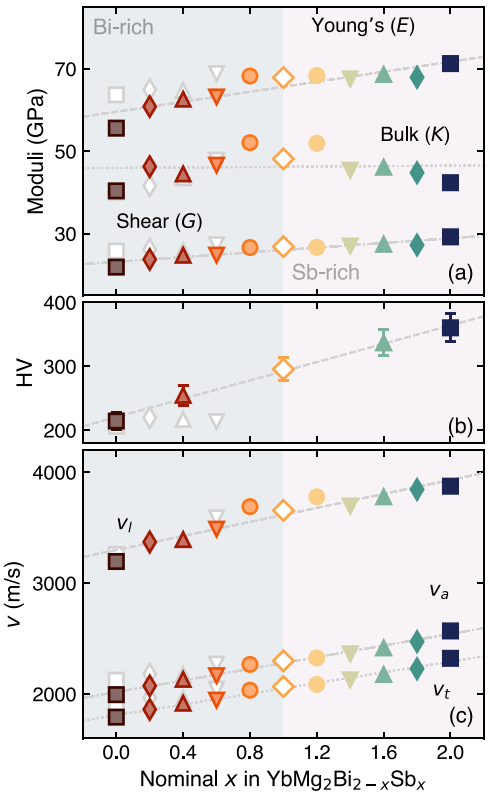

Figure 2. Evolution of (a) elastic moduli, (b) HV, and (c) sound velocities with x in $YbMg_2Bi_{2-x}Sb_x$ at room temperature. Note that the light gray lines are guides for the eye. Literature data for polycrystalline $YbMg_2Bi_{2-x-\delta}Sb_x$ ($x \leq 0.6$) reported by Liang et al. (ref 12) is also shown for comparison (open gray symbols).

and, perhaps, greater than one might expect from the 5% increase in unit cell volume. This trend also holds for the bulk and shear moduli, which increase by 13 and 57%, respectively. Although the shear-to-bulk modulus ratio increases toward Sb-rich compositions, which is typically associated with greater brittleness,[35] our experimental observations during sample handling suggest the opposite: Sb-rich samples were noticeably easier to work with, exhibiting greater compliance and resistance to fracture during polishing and cutting. This is also corroborated by a 68% increase in Vickers hardness (HV) from 214 for $YbMg_2Bi_2$ to 360 for $YbMg_2Sb_2$ (Figure 2b). As well as elastic moduli and HV, average sound velocity also increases from 1995 ms^{-1} for $YbMg_2Bi_2$ to 2786 ms^{-1} for $YbMg_2Sb_2$, demonstrating an ≈40% enhancement (Figure 2c).[36] Together, this indicates a clear tendency toward stronger bonds in Sb-rich $YbMg_2Bi_{2-x}Sb_x$, which may be attributed to the greater electronegativity difference ($\Delta\chi$) and thus higher Pauling bond dissociation energy of Mg–Sb bonds ($\Delta\chi$ = 0.66, 3.0 eV) compared with Mg–Bi bonds ($\Delta\chi$ = 0.3, 1.9 eV).[15] The increase in the Pauling bond dissociation energy and ionicity of chemical bonding undoubtedly affect both the electronic and thermal transport properties, which will be discussed in detail in the following sections.

Temperature-Dependent Thermoelectric Properties. For $YbMg_2Bi_{2-x}Sb_x$ samples with $x \leq 1$, σ exhibits a metal-like temperature dependence (Figure 3a), as expected for degenerate semiconductors.[37] This also correlates with the Seebeck coefficient α, which increases almost linearly with temperature and remains below 200 μVK^{-1} across the entire temperature range studied (Figure 3b). In contrast, samples with $x > 1$ show thermally activated transport behavior, as evidenced by the decrease in σ with temperature and the corresponding increase in the absolute values of α, indicating nondegenerate transport behavior (Figure 3a,b). In turn, the increase in the maximum Seebeck coefficient (S_{max}) and its shift toward lower temperatures with increasing Sb content signifies an increase of the band gap E_g, according to the Goldsmid–Sharp relation, $E_g = 2eS_{max}T_{max}$.[38] The corresponding values of the thermal E_g, obtained from the temperature dependence of the Seebeck coefficient (Figure 3b), 0.21 eV for $YbMg_2Bi_2$, 0.31 eV for $YbMg_2BiSb$, and 0.38 eV for $YbMg_2Sb_2$, are in good agreement with the previous studies[18,39] and confirm the gradual increase in band gap with Sb substitution. The power factor for all of the samples (Figure 3c) is calculated using the experimental α and σ values across the entire temperature range. The power factor shows an increasing trend with temperature and then saturates at higher temperatures for compositions up to x = 0.8, while for compositions beyond this, $\alpha^2\sigma$ increases monotonically over the entire temperature range. The temperature dependence of $\alpha^2\sigma$ follows that of α, while the change in magnitude with temperature closely resembles the changes occurring in σ with T.

The total thermal conductivity κ_{tot} gradually decreases with temperature (Figure 3d), as expected.[36] The maximum values of κ_{tot} are observed for the two end compositions among the series of synthesized $YbMg_2Bi_{2-x}Sb_x$ samples, while a significant drop in thermal conductivity is obtained for the remaining compositions. The lattice thermal conductivity κ_{lat} of $YbMg_2Bi_2$ and $YbMg_2Sb_2$, in turn, exhibits a $\sim T^{-1}$ temperature dependence, while the remaining intermediate compositions follow a $\sim T^{-0.5}$ temperature dependence (Figure 3e), signifying the changing scattering mechanism in the solid–solution compositions over the pristine samples, as discussed in detail below. Although there is a decline in both the power factor and thermal conductivity in Sb-substituted samples, the degree of reduction for κ_{lat} outperforms the reduction in $\alpha^2\sigma$, resulting in the highest zT for the x = 0.2 composition. Overall, zT for all of the samples shows a steady increase with temperature, with the highest $zT \approx 0.9$ at 723 K achieved for the $YbMg_2Bi_{1.8}Sb_{0.2}$ sample. Across the compositional range examined, the zT values reported in this work are generally consistent with those from previous studies by Wang et al.[11] and Liang et al.,[12] especially at room temperature, where all three studies show similar performance with only

https://doi.org/10.1021/acs.chemmater.5c01433
Chem. Mater. 2025, 37, 6782–6790

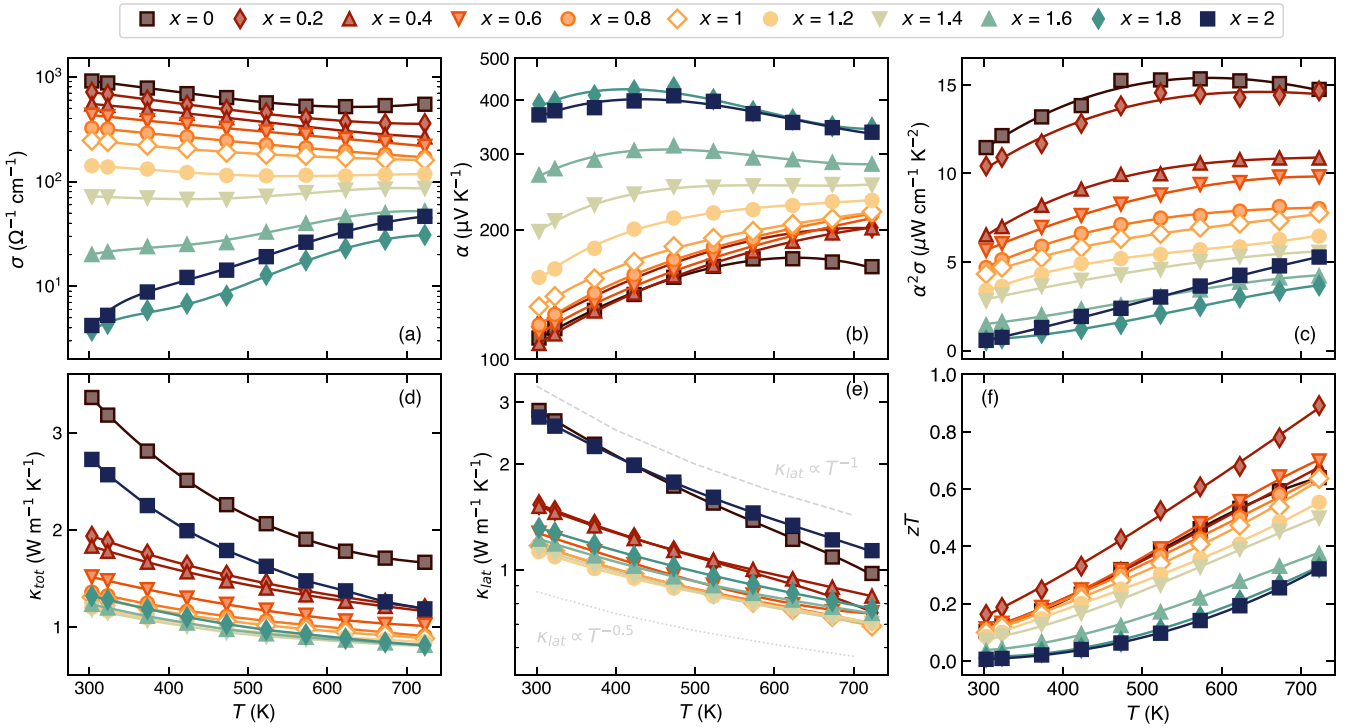

Figure 3. Temperature dependence of the (a) electrical conductivity σ, (b) Seebeck coefficient α, (c) power factor $\alpha^2\sigma$, (d) total κ_{tot} and (e) lattice κ_{lat} thermal conductivities, and (f) the figure of merit zT for $YbMg_2Bi_{2-x}Sb_x$ (x = 0, 0.2, 0.4, 0.6, 0.8, 1, 1.2, 1.4, 1.6, 1.8, 2) samples.

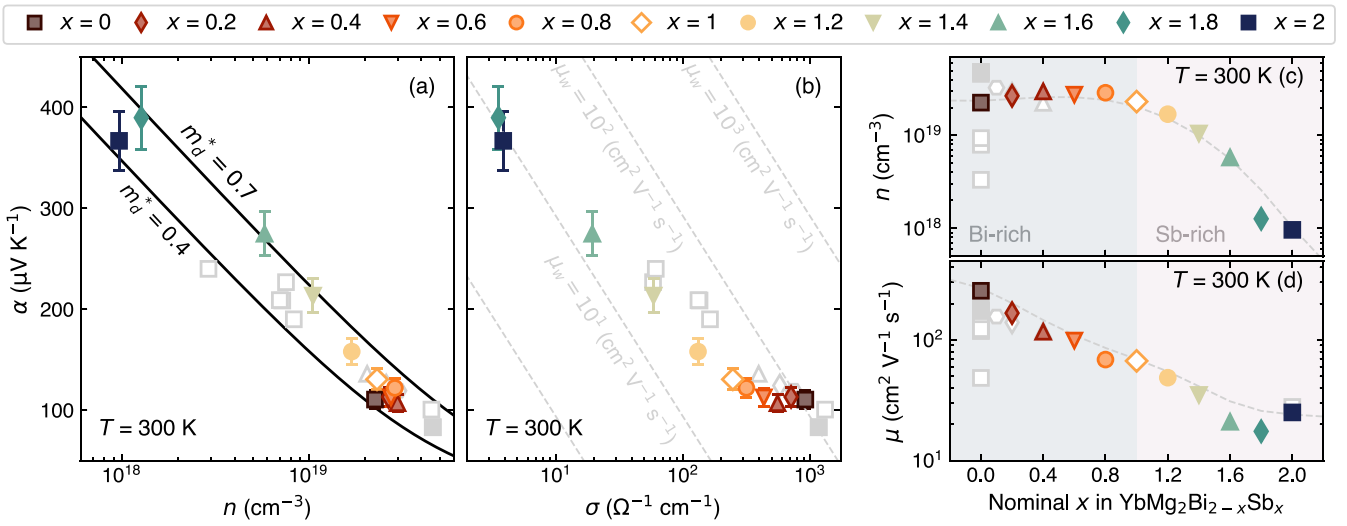

Figure 4. Seebeck coefficient α of $YbMg_2Bi_{2-x}Sb_x$ samples (a) versus charge carrier concentration n (Pisarenko plot) and (b) logarithm of electrical conductivity σ (Jonker plot) at room temperature. The solid lines in part (a) represent the Seebeck coefficient calculated in the framework of the effective mass model,[37] assuming acoustic phonon scattering ($r = -1/2$), $m_d^* = 0.4$, and $m_d^* = 0.7$, respectively. The dashed lines in part (b) represent the Pisarenko formula for different weighted mobility values (μ_w in cm^2 V^{-1} s^{-1}),[40] each labeled next to its corresponding line at the bottom part of the figure. Evolution of charge carrier (c) concentration n and (d) mobility μ with x in $YbMg_2Bi_{2-x}Sb_x$ at room temperature. The light gray lines in parts (c) and (d) are guides to the eye. Literature data for other $YbMg_2Bi_{2-x}Sb_x$ ($0 \le x \le 0.4$) reported previously (refs 10,11,18,19,24−26) is also shown for comparison (open gray symbols for polycrystals and filled gray symbols for single crystals, respectively).

minor variation (Figure S7f). At an elevated temperature (723 K), the reported data in this work not only maintains overall agreement with literature but also demonstrates a slightly higher zT for the composition with x = 0.2, reaching ≈0.9 (Figure S8). These observations underscore the reproducibility of thermoelectric trends across various studies, considering the uncertainty in zT estimation.[30]

Composition-Dependent Electrical Properties. We analyzed and compared the electronic properties of our data by using an effective mass model assuming a single parabolic band transport limited by acoustic phonon scattering at room temperature. The Pisarenko plot (Figure 4a) shows a clear shift toward higher effective masses as Bi is progressively replaced with Sb. The increasing density of states effective mass (m_d^*) reveals the possible evolution of the band structure upon Bi

https://doi.org/10.1021/acs.chemmater.5c01433
Chem. Mater. 2025, 37, 6782−6790

substitution with Sb. This is further supported by the Jonker plot (Figure 4b), which deviates from the expected slope of $-86.291\ \mu VK^{-1}$ (shift toward lower weighted mobility; μ_w) for acoustic phonon-limited scattering, indicating changes in the band structure and/or scattering mechanisms.[40] The fact that carrier mobility (μ) is inversely proportional to band effective mass (m_b^*) through $\mu \propto (m_b^*)^{-5/2}$ suggests that the decrease in mobility is due to an increase in m_b^* with increasing x. Therefore, according to the relation $m_d^* = N_v^{2/3} m_b^*$, the DOS effective mass (m_d^*) should also increase with increasing m_b^*, i.e., with increasing Sb content, as is observed in Figure 4a. The increasing m_d^* values with increasing Sb content is also supported by the insights drawn from previous DFT calculations on $YbMg_2Bi_2$ and $YbMg_2Sb_2$ systems, where $YbMg_2Bi_2$ is identified as a direct band gap semiconductor with a smaller effective mass ($m^* = 0.6$) compared to the Sb-based system ($m^* = 1$).[18,39]

Interestingly, a subtle change in the Seebeck coefficient for compositions $0 < x \leq 1$ ($110\ \mu VK^{-1}$ for $x = 0$ to $130\ \mu VK^{-1}$ for $x = 1$) followed by significant changes in α for compositions beyond $x = 1$ ($158\ \mu VK^{-1}$ at $x = 1.2$ to $366\ \mu VK^{-1}$ at $x = 2$) (Figure 4a,b) can be attributed to corresponding changes in the charge carrier concentration (n), as shown in Figure 4c, where no change in the order of n is observed for Bi-rich compositions while a significant reduction follows for the Sb-rich compositions, thus influencing the trend in α with Sb content at room temperature. The decrease in charge carrier concentration, though not monotonically, upon Sb content can be mainly attributed to the increase of the band gap, accompanied by the increasing electronegativity difference between the cation (Yb^{2+}) and the anionic framework $[Mg_2(Bi,Sb)_2]^{2-}$. In addition to this, the influence of secondary phases, in particular elemental Bi, cannot be excluded. The reduction of elemental Bi fraction (Figure 1b), along with the increase in the band gap, may affect the defect energetics, thereby contributing to the decrease in charge carrier concentration.[32] Thus, the observed trend in charge carrier concentration likely reflects the combined influence of evolution in the electronic structure and native defect energetics. To provide a more reliable confirmation of the increase in band gap, E_g, we used the Goldsmid−Sharp relation,[38] $E_g = 2eS_{max}T_{max}$, to estimate thermal E_g from the Seebeck coefficient data (Figure 3b). While this method may underestimate the magnitude of E_g,[41] it can capture the trend within a series of samples. Correspondingly, the estimated E_g for $YbMg_2Bi_2$, $YbMg_2BiSb$, and $YbMg_2Sb_2$ are 0.21, 0.31, and 0.38 eV, respectively, confirming the expected trend. Moreover, the increase in electronegativity difference of Mg−Sb bond ($\Delta\chi = 0.66$) compared to that of Mg−Bi ($\Delta\chi = 0.3$) contributes to a decrease in carrier mobility[6,15,19] (μ), as shown in Figure 4d.

Figure S6 shows an increasing trend in the effective mass (m_d^*) with x, where a small but prominent peak in m_d^* was observed for the composition $YbMg_2Bi_{0.6}Sb_{1.4}$. At this point, it is important to note that most studies on AM_2X_2 compounds assume acoustic phonon scattering (APS) as the dominant carrier scattering mechanism when analyzing electronic transport properties.[10,18] However, some works have doubted the dominance of APS, suggesting that it may not fully capture the charge carrier transport behavior in these systems.[25] Moreover, there is a growing body of work suggesting polar optical phonon (POP) scattering as the dominant mechanism in many materials.[42,43] Correspondingly, we calculated the effective mass by assuming both APS and POP mechanisms for comparison. As shown in Figure S6, although the absolute values of the extracted effective mass differ, the overall trend, i.e., the increase of m_d^* with increasing Sb content, remains the same. This increase in m_d^* with rising x can be interpreted in terms of the crystal field-induced orbital splitting.[44] The AM_2X_2 Zintl compounds have the p-orbitals of the anions dominating their valence band edge with an offset in the energy (Δ) of p_z and (p_x, p_y) orbitals owing to the effect of crystal field splitting, meaning that there is a separation between these two sets of orbitals on the energy scale. As the lattice parameters a and c decrease with x (Figure 1c,d), the crystal field splitting energy (Δ) should also vary, indicating that the magnitude of separation (Δ) between the two sets of orbitals will vary. Considering Δ dependence on a for several AM_2X_2 compounds, one may expect Δ to be more negative on the energy scale for $YbMg_2Sb_2$ than $YbMg_2Bi_2$.[44] A more negative Δ value signifies a higher energy offset between the p_z and (p_x, p_y) orbitals at the Γ-symmetry point in the band structure. This implies that the difference in the energy of p_z and (p_x, p_y) orbitals of $YbMg_2Bi_2$ is less compared to the difference in the energy for the same set of orbitals of $YbMg_2Sb_2$. Therefore, we can presume the (p_x, p_y) orbitals of $YbMg_2Bi_2$ to be closer to the valence band maxima (VBM) compared to the (p_x, p_y) orbitals of $YbMg_2Sb_2$. Hence, with the increase in Sb content in the pristine composition $YbMg_2Bi_2$, it can be expected that the energy difference between the p_z and (p_x, p_y) orbitals of $YbMg_2Bi_2$ will slowly increase, shifting the (p_x, p_y) orbitals toward a more negative energy scale. Due to an alloy composition, it is very much feasible that the shifts in (p_x, p_y) orbitals of pure Bi-based composition will eventually lead it to an overlap with the p_z and/or (p_x, p_y) orbitals of Sb-rich compositions at some intermediate value of x in $YbMg_2Bi_{2-x}Sb_x$. This speculated gradual shifting of one set of orbitals toward the other set of p_z/(p_x, p_y) orbitals, pushing it toward an orbital overlap state, will gradually lead to an increase in the overall band effective mass (m_b^*) and thus an increase in the m_d^*, followed by a simultaneous increase in the Seebeck coefficient, supporting the experimentally observed increasing trend in α while a decreasing trend in μ with x (Figure 4).

Composition-Dependent Thermal Transport. The total thermal conductivity (κ_{tot}) of all samples was measured, revealing a significant reduction of approximately 61% at room temperature, e.g., from 3.36 $Wm^{-1}K^{-1}$ for $YbMg_2Bi_2$ to 1.20 $Wm^{-1}K^{-1}$ for $YbMg_2Bi_{0.8}Sb_{1.2}$ composition. Beyond $x = 1.2$, the thermal conductivity gradually increases (Figure 3d). A similar compositional trend was observed in the room-temperature lattice thermal conductivity (κ_{lat}), as shown in Figure 5. Lattice thermal conductivity values of 2.8 $Wm^{-1}K^{-1}$ and 2.7 $Wm^{-1}K^{-1}$ for the end-members $YbMg_2Bi_2$ and $YbMg_2Sb_2$, respectively, are in agreement with the reported values.[26,45] Compositional dependence of the κ_{lat} was further analyzed by employing the Klemens model.[46] The model accounts for the disorder scaling parameter (u) obtained from the following equation.

$$\frac{\kappa_{lat}}{\kappa_{lat}^0} = \frac{\tan^{-1} u}{u} \tag{3}$$

which includes the disorder scattering parameter (Γ) related to u as

https://doi.org/10.1021/acs.chemmater.5c01433
Chem. Mater. 2025, 37, 6782−6790

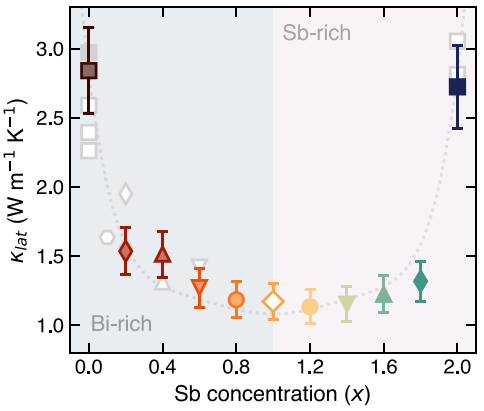

Figure 5. Lattice thermal conductivity of the $YbMg_2Bi_{2-x}Sb_x$ solid solution. The dotted line shows the predicted reduction in κ_{lat} from the Klemens model (eq 3) at 300 K. Literature data for $YbMg_2Bi_{2-x}Sb_x$ reported previously (refs11,12,18,19,25,26.) is also shown for comparison.

$$u^2 = \frac{\pi^2 \theta_D V_{at}}{h v_a^2} \kappa_{lat}^0 \Gamma \tag{4}$$

where κ_{lat}^0 is the lattice thermal conductivity of the pristine sample (i.e., $YbMg_2Bi_2$), κ_{lat} is the lattice thermal conductivity of the Sb-substituted samples, h is Planck's constant, θ_D is the Debye temperature, V_{at} is the volume per atom, and v_a is the average velocity of sound for Sb-substituted compositions, respectively. The obtained values of u and Γ are listed in Table S3. A reasonable fit for κ_{lat} is achieved, as shown in Figure 5, suggesting that point-defect scattering plays a central role in the thermal transport of the solid solution system. The trend in the obtained fitting parameters u and Γ suggests that the mass and strain fluctuation arising due to the Sb substitution at the Bi site plays a vital role in the thermal conductivity of alloyed compositions.

CONCLUSIONS

We report the first successful synthesis and systematic investigation of the full solid solution series $YbMg_2Bi_{2-x}Sb_x$ ($0 \le x \le 2$), a case study of anion-site substitution in the AM_2X_2 Zintl phases. The primary aim of achieving a mechanically tough/stable system with substituting more electronegative element at the anion site is successfully realized over the full range of composition, as we shift from a weakly bonded structure of $YbMg_2Bi_2$ to a strong bonding network of $YbMg_2Sb_2$, as supported by the increasing elastic moduli values with Sb content. A comprehensive analysis of the transport properties supported by the room temperature Hall measurements has been discussed in order to understand the mechanism behind the evolution of thermoelectric properties upon Sb content. A gradual increase observed in the effective mass (m_d^*) leads to the monotonic decrease of carrier mobility (μ) with Sb content, which is also supported by the observed increase of electronegativity. Changes occurring in the bonding orbitals at the VBM due to the difference in crystal field splitting energy in the two end compositions, $YbMg_2Bi_2$ and $YbMg_2Sb_2$, lead to orbital overlap at an intermediate composition of $YbMg_2Bi_{0.4}Sb_{1.6}$. The enhancement in m_d^* is consistent with the increase in the orbital overlap arising from compositional tuning. Though the power factor decreases monotonically with x, the sudden drop (almost 3 times) in κ_{lat} for $YbMg_2Bi_{1.8}Sb_{0.2}$ from the pristine composition improves its efficiency, resulting in a $zT \approx 0.9$ at 723 K. A significantly reduced lattice thermal conductivity upon alloying is analyzed using the Klemens model, and as a result, point-defect scattering due to the increase in mass difference at the anion site is attributed to the trend of κ_{lat} with x. Overall, the current work provides insight into the complex interplay among chemical bonding, band structure, and electron transport in anion-substituted Zintl compounds. Our findings suggest that the midrange to Sb-rich compositions ($x = 1.6 - 1.8$) exhibit a favorable balance of low lattice thermal conductivity, enhanced mechanical robustness (reflected in higher elastic moduli), and high Seebeck coefficients ($\approx$400 μVK^{-1}), making them particularly promising for targeted doping strategies aimed at optimizing carrier concentration and further improvement of zT.

ASSOCIATED CONTENT

Data Availability Statement

Data will be made available upon request.

Supporting Information

The Supporting Information is available free of charge at https://pubs.acs.org/doi/10.1021/acs.chemmater.5c01433.

XRD data of samples prepared with different ball milling time and corresponding temperature-dependent electrical and thermal transport properties of those samples, relative density and lattice parameters for all $YbMg_2Bi_{2-x}Sb_x$ samples, Rietveld refinement fits for $YbMg_2Bi_2$, YbMg$_2$BiSb, and $YbMg_2Sb_2$, SEM images for the same compositions, evolution of the effective mass with Sb content, fit parameters of Klemens model and room temperature thermoelectric properties of solid solution $YbMg_2Bi_{2-x}Sb_x$ upon Sb content, and compositional dependence of zT at 723 K (PDF)

AUTHOR INFORMATION

Corresponding Authors

Andrei Novitskii − *Research Center for Materials Nanoarchitectonics (MANA), National Institute for Materials Science (NIMS), Tsukuba, Ibaraki 305-0044, Japan*; Email: NOVITSKII.Andrei@nims.go.jp

Takao Mori − *Research Center for Materials Nanoarchitectonics (MANA), National Institute for Materials Science (NIMS), Tsukuba, Ibaraki 305-0044, Japan; Graduate School of Pure and Applied Sciences, University of Tsukuba, Tsukuba, Ibaraki 305-8573, Japan*; orcid.org/0000-0003-2682-1846; Email: MORI.Takao@nims.go.jp

Author

Kushal Mehrotra − *Research Center for Materials Nanoarchitectonics (MANA), National Institute for Materials Science (NIMS), Tsukuba, Ibaraki 305-0044, Japan; Graduate School of Pure and Applied Sciences, University of Tsukuba, Tsukuba, Ibaraki 305-8573, Japan*

Complete contact information is available at: https://pubs.acs.org/10.1021/acs.chemmater.5c01433

Author Contributions

K.M.: Investigation, formal analysis, visualization, writing—original draft, and writing—review and editing. A.N.: Conceptualization, investigation, formal analysis, methodology,

https://doi.org/10.1021/acs.chemmater.5c01433
Chem. Mater. 2025, 37, 6782−6790

visualization, writing—original draft, and writing—review and editing. T.M.: Resources, funding acquisition, supervision, and writing—review and editing.

Notes

The authors declare no competing financial interest.

■ ACKNOWLEDGMENTS

This work was supported by JST Mirai JPMJMI19A1. K.M. acknowledges the financial support provided by the Japanese Government (Monbukagakusho) Scholarship (MEXT scholarship). A part of this work was supported by "Advanced Research Infrastructure for Materials and Nanotechnology in Japan (ARIM)" of the Ministry of Education, Culture, Sports, Science and Technology (MEXT) Proposal Number JPMXP1224NM5121.

■ REFERENCES

(1) Snyder, G. J.; Toberer, E. S. Complex Thermoelectric Materials. *Nat. Mater.* **2008**, *7*, 105−114.
(2) Snyder, G. J.; Snyder, A. H. Figure of Merit ZT of a Thermoelectric Device Defined from Materials Properties. *Energy Environ. Sci.* **2017**, *10*, 2280−2283.
(3) Ioffe, A. F. *Semiconductor Thermoelements, and Thermoelectric Cooling*; Infosearch: London, 1957.
(4) Kazem, N.; Kauzlarich, S. M. *Handbook on the Physics and Chemistry of Rare Earths*; Elsevier, 2016; Vol. *50*, pp 177−208.
(5) Kauzlarich, S. M. Zintl Phases: From Curiosities to Impactful Materials. *Chem. Mater.* **2023**, *35*, 7355−7362.
(6) Peng, W.; Chanakian, S.; Zevalkink, A. Crystal Chemistry and Thermoelectric Transport of Layered AM_2X_2 Compounds. *Inorg. Chem. Front.* **2018**, *5*, 1744−1759.
(7) Kauzlarich, S. M.; Zevalkink, A.; Toberer, E.; Snyder, G. J. *Zintl Phases: Recent Developments in Thermoelectrics and Future Outlook*, Energy and Environment Series; RSC, 2016; Chapter 1, pp 1−26.
(8) Liu, Z.; Sato, N.; Gao, W.; Yubuta, K.; Kawamoto, N.; Mitome, M.; Kurashima, K.; Owada, Y.; Nagase, K.; Lee, C.-H.; Yi, J.; Tsuchiya, K.; Mori, T. Demonstration of Ultrahigh Thermoelectric Efficiency of ∼ 7.3% in Mg_3Sb_2/MgAgSb Module for Low-Temperature Energy Harvesting. *Joule* **2021**, *5*, 1196−1208.
(9) Imasato, K.; Wood, M.; Anand, S.; Kuo, J. J.; Snyder, G. J. Understanding the High Thermoelectric Performance of Mg_3Sb_2−Mg_3Bi_2 Alloys, Adv. *Energy Sustainability Res.* **2022**, *3*, No. 2100208.
(10) Shuai, J.; Geng, H.; Lan, Y.; Zhu, Z.; Wang, C.; Liu, Z.; Bao, J.; Chu, C.-W.; Sui, J.; Ren, Z. Higher Thermoelectric Performance of Zintl Phases $(Eu_{0.5}Yb_{0.5})_{1-x}Ca_xMg_2Bi_2$ by Band Engineering and Strain Fluctuation. *Proc. Natl. Acad. Sci. U.S.A.* **2016**, *113*, E4125−E4132.
(11) Wang, J.; Guo, M.; Zhu, J.; Qin, D.; Guo, F.; Zhang, Q.; Cai, W.; Sui, J. Enhanced Thermoelectric Properties of Zintl Phase $YbMg_2Bi_{1.98}$ through Bi Site Substitution with Sb. *J. Mater. Sci. Technol.* **2020**, *59*, 189−194.
(12) Liang, Z.; Shang, H.; Xu, C.; Shi, X.; Zhang, F.; Ren, W.; Song, S.; Ding, F.; Ren, Z. New Insights into the Effect of Chemical Bonding Strength on Thermoelectric Performance and Stability in $YbMg_2Bi_2$ toward Practical Thermoelectric Applications. *Mater. Today Phys.* **2022**, *28*, No. 100858.
(13) Isotta, E.; Peng, W.; Balodhi, A.; Zevalkink, A. Elastic Moduli: A Tool for Understanding Chemical Bonding and Thermal Transport in Thermoelectric Materials. *Angew. Chem., Int. Ed.* **2023**, *62* (12), No. e202213649.
(14) Shannon, R. D. Revised Effective Ionic Radii and Systematic Studies of Interatomic Distances in Halides and Chalcogenides. *Acta Crystallogr., Sect. A* **1976**, *32*, 751−767.
(15) Tantardini, C.; Oganov, A. R. Thermochemical Electronegativities of the Elements. *Nat. Commun.* **2021**, *12*, No. 2087.
(16) Hanus, R.; Agne, M. T.; Rettie, A. J.; Chen, Z.; Tan, G.; Chung, D. Y.; Kanatzidis, M. G.; Pei, Y.; Voorhees, P. W.; Snyder, G. J. Lattice Softening Significantly Reduces Thermal Conductivity and Leads to High Thermoelectric Efficiency. *Adv. Mater.* **2019**, *31*, No. 1900108.
(17) Slade, T. J.; Anand, S.; Wood, M.; Male, J. P.; Imasato, K.; Cheikh, D.; Al Malki, M. M.; Agne, M. T.; Griffith, K. J.; Bux, S. K.; Wolverton, C.; Kanatzidis, M. G.; Snyder, G. J. Charge-Carrier-Mediated Lattice Softening Contributes to High zT in Thermoelectric Semiconductors. *Joule* **2021**, *5*, 1168−1182.
(18) Zhou, T.; Feng, Z.; Mao, J.; Jiang, J.; Zhu, H.; Singh, D. J.; Wang, C.; Ren, Z. Thermoelectric Properties of Zintl Phase $YbMg_2Sb_2$. *Chem. Mater.* **2020**, *32*, 776−784.
(19) Zhang, Z.; Wang, X.; Liu, Y.; Chen, C.; Yao, H.; Yin, L.; Li, X.; Li, S.; Zhang, F.; Bai, F.; Sui, J.; Yu, B.; Cao, F.; Liu, X.; Mao, J.; Xie, G.; Zhang, Q. Balancing the Anionic Framework Polarity for Enhanced Thermoelectric Performance in $YbMg_2Sb_2$ Zintl Compounds. *J. Materiomics* **2019**, *5*, 583−589.
(20) Rodríguez-Carvajal, J. Recent Advances in Magnetic Structure Determination by Neutron Powder Diffraction. *Phys. B* **1993**, *192*, 55−69.
(21) Ashcroft, N. W.; Mermin, N. D.Solid State Physics HarcourtCollege Publishers, 1976.
(22) Kittel, C. *Introduction to Solid State Physics*, 8th ed.; Wiley, 2004.
(23) Gurunathan, R.; Hanus, R.; Snyder, G. J. Alloy scattering of phonons. *Mater. Horiz.* **2020**, *7*, 1452−1456.
(24) May, A. F.; McGuire, M. A.; Singh, D. J.; Custelcean, R.; Jellison, G. E., Jr Structure and Properties of Single Crystalline $CaMg_2Bi_2$, $EuMg_2Bi_2$, and $YbMg_2Bi_2$. *Inorg. Chem.* **2011**, *50*, 11127−11133.
(25) May, A. F.; McGuire, M. A.; Singh, D. J.; Ma, J.; Delaire, O.; Huq, A.; Cai, W.; Wang, H. Thermoelectric Transport Properties of $CaMg_2Bi_2$, $EuMg_2Bi_2$, and $YbMg_2Bi_2$. *Phys. Rev. B* **2012**, *85*, No. 035202.
(26) Shuai, J.; Liu, Z.; Kim, H. S.; Wang, Y.; Mao, J.; He, R.; Sui, J.; Ren, Z. Thermoelectric Properties of Bi-based Zintl Compounds $Ca_{1-x}Yb_xMg_2Bi_2$. *J. Mater. Chem. A* **2016**, *4*, 4312−4320.
(27) Cape, J. A.; Lehman, G. Temperature and Finite Pulse-Time Effects in the Flash Method for Measuring Thermal Diffusivity. *J. Appl. Phys.* **1963**, *34*, 1909−1913.
(28) Agne, M. T.; Imasato, K.; Anand, S.; Lee, K.; Bux, S. K.; Zevalkink, A.; Rettie, A. J.; Chung, D. Y.; Kanatzidis, M. G.; Snyder, G. J. Heat Capacity of Mg_3Sb_2, Mg_3Bi_2, and Their Alloys at High Temperature. *Mater. Today Phys.* **2018**, *6*, 83−88.
(29) Kim, H.-S.; Gibbs, Z. M.; Tang, Y.; Wang, H.; Snyder, G. J. Characterization of Lorenz Number with Seebeck Coefficient Measurement. *APL Mater.* **2015**, *3*, No. 041506.
(30) Alleno, E.; Bérardan, D.; Byl, C.; Candolfi, C.; Daou, R.; Decourt, R.; Guilmeau, E.; Hébert, S.; Hejtmánek, J.; Lenoir, B.; Masschelein, P.; Ohorodnichuk, V.; Pollet, M.; Populoh, S.; Ravot, D.; Rouleau, O.; Soulier, M. A Round Robin Test of the Uncertainty on the Measurement of the Thermoelectric Dimensionless Figure of Merit of $Co_{0.97}Ni_{0.03}Sb_3$,. *Rev. Sci. Instrum.* **2015**, *86*, No. 011301.
(31) Wang, J.; Guo, F.; Guo, M.; Zhu, J.; Zhang, Q.; Cai, W.; Sui, J. Zintl Phase $Yb_{1-x}Ba_xMg_2Bi_{1.98}$ Compounds with Enhanced Thermoelectric Performance Caused by Cation Substitution. *ACS Appl. Energy Mater.* **2020**, *3*, 11036−11041.
(32) Guo, M.; Zhai, W.; Li, J.; Zhu, J.; Guo, F.; Liu, Z.; Liu, M.; Zhu, Y.; Dong, X.; Zhang, Y.; Zhang, Q.; Cai, W.; Sui, J. High Thermoelectric Performance of $CaMg_2Bi_2$ Enabled by Dynamic Doping and Orbital Alignment. *Adv. Funct. Mater.* **2022**, *32*, No. 2200407.
(33) WebElements, "Periodic Table of the Elements" 2024. https://www.webelements.com/, (accessed February 2024).
(34) Zeier, W. G.; Heinrich, C. P.; Day, T.; Panithipongwut, C.; Kieslich, G.; Brunklaus, G.; Snyder, G. J.; Tremel, W. Bond Strength Dependent Superionic Phase Transformation in the Solid Solution Series $Cu_2ZnGeSe_{4-x}S_x$. *J. Mater. Chem. A* **2014**, *2*, 1790−1794.
(35) Thompson, R.; Clegg, W. Predicting Whether a Material is Ductile or Brittle. *Curr. Opin. Solid State Mater. Sci.* **2018**, *22*, 100−108.

https://doi.org/10.1021/acs.chemmater.5c01433
Chem. Mater. 2025, 37, 6782−6790

(36) Tritt, T. M. *Thermal Conductivity*; Springer: New York, 2010.
(37) Fistul, V. I. *Heavily Doped Semiconductors*; Plenum Press, 1969.
(38) Goldsmid, H. J.; Sharp, J. Estimation of the Thermal Band Gap of a Semiconductor from Seebeck Measurements. *J. Electron. Mater.* **1999**, *28*, 869−872.
(39) Zhang, J.; Song, L.; Madsen, G. K.; Fischer, K. F.; Zhang, W.; Shi, X.; Iversen, B. B. Designing High-Performance Layered Thermoelectric Materials Through Orbital Engineering. *Nat. Commun.* **2016**, *7*, No. 10892.
(40) Novitskii, A.; Mori, T. Pisarenko's Formula for the Thermopower. 2025 arXiv:2502.03837. arXiv.org e-Print archive. https://arxiv.org/abs/2502.03837.
(41) Gibbs, Z. M.; Kim, H.-S.; Wang, H.; Snyder, G. J. Band gap estimation from temperature dependent Seebeck measurement−Deviations from the 2e|SlmaxTmax relation. *Appl. Phys. Lett.* **2015**, *106*, No. 022112.
(42) Ganose, A. M.; Park, J.; Faghaninia, A.; Robinson, R. W.; Persson, K. A.; Jain, A. Efficient Calculation of Carrier Scattering Rates from First Principles. *Nat. Commun.* **2021**, *12*, No. 2222, DOI: 10.1038/s41467-021-22440-5.
(43) Guo, M.; Liu, M.; Yuan, D.; Chen, H.; Sun, C.; Zhang, Q.; Zhu, Y.; Guo, F.; Yu, Y.; Sui, J. Strong Polar Optical Phonon Screening and Softening Enhance the Thermoelectric Performance of Zintl Compounds. *Adv. Energy Mater.* **2025**, *15*, No. 2405024.
(44) Zhang, J.; Song, L.; Madsen, G. K. H.; Fischer, K. F. F.; Zhang, W.; Shi, X.; Iversen, B. B. Designing High-Performance Layered Thermoelectric Materials Through Orbital Engineering. *Nat. Commun.* **2016**, *7*, No. 10892.
(45) Zhou, T.; Feng, Z.; Mao, J.; Jiang, J.; Zhu, H.; Singh, D. J.; Wang, C.; Ren, Z. Thermoelectric properties of zintl phase $YbMg_2Sb_2$. *Chem. Mater.* **2020**, *32*, 776−784.
(46) Klemens, P. G. Thermal Resistance due to Point Defects at High Temperatures. *Phys. Rev.* **1960**, *119*, No. 507.

https://doi.org/10.1021/acs.chemmater.5c01433
Chem. Mater. 2025, 37, 6782−6790